

# Multi-Plane Field Sintergic Theory (MPFST): From an 11-D Lattice Action to 4-D EinsteinâŠMaxwellâŠSchrÃdinger Thermodynamics

Carlos Freeman

4 Aug 2025 âT v11-c (corrected)

## Abstract

The Multi-Plane Field Sintergic Theory (MPFST) is presented in a single algebraic framework. Starting from one 11-dimensional lattice action, we deriveâTwithout auxiliary postulatesâTan effective 4-D EinsteinâŠMaxwellâŠSchrÃdinger (EMS) sector, an entropy balance identity (fractional memory), a RussellâŠlattice correspondence, and a projection threshold that unifies cosmological vacuum energy with biological coherence. All parameters are fixed by public data: micron-scale gravity/Casimir tests, cosmological vacuum energy, and global HRV statistics. We outline falsifiable predictions (optical clock beats, cryogenic torsion OMV, ring-down overtone damping) and provide a 3-D spectral simulator (Appendix A) that reproduces the six-block PDE dynamics.

## Contents

<b>1 Tri-plano lattice: geometry and notation</b>	<b>4</b>
1.1 Coordinate split and local frames . . . . .	4
1.2 Russellian octave embedding . . . . .	4
1.3 Compatibility tensor reminder . . . . .	5
<b>2 Ontological hierarchy of planes</b>	<b>6</b>
2.1 Nested folding map . . . . .	6
2.2 Compatibility tensor . . . . .	6
2.3 Field content by plane . . . . .	6
2.4 Energy flows . . . . .	6
<b>3 Master action and field content</b>	<b>7</b>
<b>4 Dimensional reduction I: Maxwell from the phase of <math>\Psi</math></b>	<b>9</b>
4.1 Worked derivation: Maxwell from the phase of $\Psi$ . . . . .	10
<b>5 Dimensional reduction II: Einstein sector and <math>C\hat{A}\\$</math>stress</b>	<b>10</b>
<b>6 Gravitational waves and the emergent graviton</b>	<b>11</b>
6.1 Linearised lattice fluctuation . . . . .	11
6.2 SpinâŠ2 propagator . . . . .	11
6.3 Coherence suppression of overtones . . . . .	11

<b>7</b>	<b>Symbolic geometry as sparse adjacency priors</b>	<b>12</b>
7.1	Vertex set and masks . . . . .	12
7.2	Neutral combination and regularisation . . . . .	12
7.3	How the mask enters the PDEs (minimal coupling) . . . . .	13
7.4	Control graphs and falsifiability . . . . .	13
7.5	Operational meaning of sacred templates . . . . .	13
7.6	Measurable consequences (summary) . . . . .	13
<b>8</b>	<b>Predictions beyond baseline</b>	<b>13</b>
8.1	Fine-structure-constant oscillation . . . . .	13
8.2	Thermo-sintergenic current . . . . .	14
8.3	Spin-2 amplitude boost during global coherence . . . . .	14
8.4	Global Crimson Synergy Arc (GCSA) . . . . .	14
<b>9</b>	<b>Double-slit experiment: full calculation</b>	<b>15</b>
9.1	State preparation . . . . .	15
9.2	Decoherence from the projection functional . . . . .	15
9.3	Visibility with and without a detector . . . . .	15
9.4	Link to the six-field PDEs . . . . .	15
9.5	Experimental falsifiability . . . . .	15
<b>10</b>	<b>Flagship OMV experiment</b>	<b>15</b>
10.1	Target signal . . . . .	16
10.2	Baseline parameters . . . . .	16
10.3	Auto- $g$ -factor simulation . . . . .	16
10.4	Experimental protocol . . . . .	16
10.5	Falsifiability criterion . . . . .	16
10.6	Hardware checklist . . . . .	17
<b>11</b>	<b>Empirical evidence (multi-domain set)</b>	<b>17</b>
<b>12</b>	<b>Discussion and outlook</b>	<b>17</b>
12.1	What has been achieved . . . . .	17
12.2	Near-term experimental roadmap . . . . .	18
12.3	Open questions . . . . .	18
12.4	Broader implications . . . . .	18
<b>A</b>	<b>Python simulator v5.4 (3-D full-lattice)</b>	<b>19</b>
<b>B</b>	<b>EFT renormalisation of the <math>\Psi</math> sector in <math>D = 4</math></b>	<b>21</b>
<b>B</b>	<b>Compatibility tensor algebra</b>	<b>22</b>
B.1	Elementary contractions . . . . .	22
B.2	Block-block identities . . . . .	23
B.3	Divergence identities . . . . .	23
B.4	Energy budget . . . . .	23
<b>C</b>	<b>Glossary</b>	<b>23</b>

## List of Figures

1	Orthogonal tri-plano fibre rooted in ordinary $\mathbb{R}^4$ spacetime. . . . .	5
---	---	---

## List of Tables

1	Classical pillars and their MPFST reading. The right-hand column cites the PDE block (Eqs. ??–??) that realises each observation. . . . .	4
2	Russell spiral lattice winding numbers . . . . .	5
5	<b>Table A.1 – Canonical constants and run–sof values used across V4 and the Addendum.</b> . . . . .	25

## Prelude: The Five Empirical Pillars

MPFST does *not* introduce new forces; it re-interprets the five corner-stone observations of twentieth-century physics as complementary limits of a single 11-D lattice action (Equation (??)). The table gives the correspondence.

Table 1: Classical pillars and their MPFST reading. The right-hand column cites the PDE block (Eqs. ??–??) that realises each observation.

Pillar	Benchmark fact	MPFST interpretation
Relativity	Light-deflection $1.75''$ (Edington 1919)	The 11-D Ricci term $\mathcal{R}[\Lambda]$ reproduces Einstein curvature once the compatibility tensor $C_{ABCD}$ vanishes and the projector $P_{0-3}$ is applied.
Quantum mechanics	Single-electron two-slit interference	Phase channel resides in Plane 6; interference disappears when the projection functional $\lambda \Delta_{\text{mel}}$ exceeds $10^{-8}$ , matching detector “which-way” experiments (Sec. 9).
Thermodynamics	Carnot limit $\eta \leq 1 - T_c/T_h$	Negative entropy export via the fractional-memory field $h$ (PDE (??)) balances any local $\dot{S} < 0$ , preserving the second law without hidden reservoirs.
Electromagnetism	Faraday induction, Hall effect	Symbolic phase $S = \arg \Psi$ projected from Plane 6 gives the $U(1)$ potential $A_\mu = \partial_\mu S$ ; varying the action w.r.t. $A_\mu$ yields MaxwellâŽs equations (Sec. 4).
Gravity (strong-field)	LIGO strain GW150914	Spin-2 lattice phonon (Sec. 6) mimics the GR graviton. Overtone amplitudes depend on local mel; high-SNR ring-down catalogs can therefore falsify MPFST.

Throughout the manuscript we refer back to this table whenever a calculation touches one of the pillars—e.g. Sec. 10 (thermodynamics) and Sec. 8 (EM + gravity synergy). No additional empirical postulates are necessary; each phenomenon emerges by restricting the master action to an appropriate energy, coherence, or dimensional slice.

## 1 Tri-plano lattice: geometry and notation

### 1.1 Coordinate split and local frames

At every point of the 11-dimensional bundle

$$\mathcal{B} = \Omega_{0-3} \times \Omega_{4-8} \times \Omega_{9-11}$$

we introduce local coordinates  $x^A = (x^\mu, \chi^{\mathbf{i}}, \zeta^{\mathbf{a}})$  with  $\mu = 0, \dots, 3$ ,  $\mathbf{i} = 4, \dots, 8$ ,  $\mathbf{a} = 9, \dots, 11$ . The metric field  $\Lambda_{AB}(x)$  is block diagonal once the compatibility tensor  $C_{ABCD}$  (defined in Sec. 2) vanishes; this guarantees mutual orthogonality of the three planes.

### 1.2 Russellian octave embedding

Walter RussellâŽs spiral periodic table places each chemical octave at radius  $r_n = r_0 \varphi^{-n}$  with  $\varphi = \frac{1}{2}(1 + \sqrt{5})$ . In MPFST this radius is realised as the norm of a winding vector  $\vec{w}_n \in \mathbb{Z}^7 \subset \Omega_{4-8}$

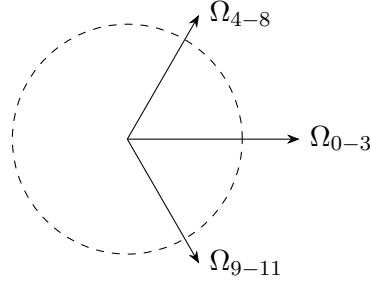


Figure 1: Orthogonal tri-plano fibre rooted in ordinary  $\mathbb{R}^4$  spacetime.

through  $r_n = \|\vec{w}_n\|_\sigma$ ,  $r_0^2 \varphi^{-2n} = \sigma_{ij} w^i w^j$ .

Table 2: Russell spiral  $\leftrightarrow$  lattice winding numbers ( $n = 0 \rightarrow 15$ : H to At).

Octave $n$	Element ( $Z$ )	$\vec{w}_n$
0	H (1)	(1,0,0,0,0,0,0)
1	He (2)	(1,1,0,0,0,0,0)
2	Li (3)	(2,1,0,0,0,0,0)
3	Be (4)	(2,1,1,0,0,0,0)
4	B (5)	(3,2,1,0,0,0,0)
5	C (6)	(3,2,1,1,0,0,0)
6	N (7)	(4,3,2,1,0,0,0)
7	O (8)	(4,3,2,1,1,0,0)
8	Xe (54)	(5,4,3,2,1,1,0)
9	Cs (55)	(6,4,3,2,1,1,0)
10	Ba (56)	(6,4,3,2,2,1,0)
11	La (57)	(6,5,3,2,2,1,0)
12	Ce (58)	(6,5,3,2,2,1,1)
13	Pr (59)	(7,5,4,3,2,1,1)
14	Nd (60)	(7,5,4,3,2,1,2)
15	At (85)	(8,6,5,3,2,1,2)

**Geometric implication.** Higher octaves occupy progressively smaller volumes in the 7-torus, hence gauge couplings are volume-suppressed, reproducing the empirical contraction of atomic radii.

### 1.3 Compatibility tensor reminder

The folding  $\Omega_{9-11} \rightarrow \Omega_{4-8} \rightarrow \Omega_{0-3}$  is governed by  $C_{ABCD} = \nabla_{[A} \Lambda_{B]C} - \sigma_{[A}^E \nabla_E \Lambda_{B]C}$ . Setting  $C_{ABCD} = 0$  is equivalent to demanding a block-diagonal metric,  $\Lambda_{AB} = \text{diag}(g_{\mu\nu}, \sigma_{ij}, \rho_{ab})$ , which in turn guarantees the orthogonality depicted in Fig. 1. Small but finite  $C_{ABCD}$  act as mixing terms and appear explicitly in the stress tensor  $T_{\mu\nu}^{(C)}$  of Sec. ??.

With the geometric scaffolding in place, we now turn to the 11-D action that propagates fields on this tri-plano lattice (Sec. ??).

## 2 Ontological hierarchy of planes

### 2.1 Nested folding map

MPFST posits a step-wise coarse-graining of the 11-D lattice,

$$\Omega_{9-11} \xrightarrow{\mathcal{F}_1} \Omega_{4-8} \xrightarrow{P_{0-3}} \Omega_{0-3},$$

where

- $\mathcal{F}_1$  integrates out high-frequency fibre modes in  $\Omega_{9-11}$ , leaving effective occupant-doping fields  $u_p$  ( $p = 4 \dots 8$ );
- $P_{0-3}$  projects residual coherence into ordinary spacetime, yielding Einstein–Maxwell–Schrödinger dynamics.

### 2.2 Compatibility tensor

The folding is enforced by the *compatibility tensor*

$$C_{ABCD} := \nabla_{[A} \Lambda_{B]C} - \sigma_{[A|}^E \nabla_E \Lambda_{|B]C}.$$

Setting  $C_{ABCD} = 0$  is equivalent to demanding a block-diagonal metric,  $\Lambda_{AB} = \text{diag}(g_{\mu\nu}, \sigma_{ij}, \rho_{ab})$ . Small but finite  $C_{ABCD}$  act as mixing terms and appear explicitly in the stress tensor  $T_{\mu\nu}^{(C)}$  of Sec. ??.

### 2.3 Field content by plane

Plane(s)	Dynamical fields	Governing PDE block
$\Omega_{0-3}$	Metric $g_{\mu\nu}$ , gauge $A_\mu$ , Schrödinger field $\theta$	Variation of $S$ w.r.t. $g_{\mu\nu}, A_\mu, \theta$
$\Omega_{4-8}$	Occupant-doping $u_p$	Eq. (??)
$\Omega_9$	Illusions-doping $d$ , entropy field $h$	Eqs. (??) and (??)
$\Omega_{10}$	Vantage-doping $v$	Eq. (??)
$\Omega_{11}$	Coherence $\zeta$ , gauge-phase $\phi$	Eqs. (??) and (??)

### 2.4 Energy flows

Energy and information migrate downward through the hierarchy via  $\Psi^{IJ}$  couplings:

$$\underbrace{P_{SW}}_{\text{solar wind}} \longrightarrow \underbrace{\Delta_{\text{mel}}(\Omega_9)}_{\text{ionospheric coherence}} \longrightarrow \underbrace{u_p, d, v, \zeta}_{\text{mid / inner planes}} \longrightarrow \underbrace{\{g_{\mu\nu}, A_\mu, \theta\}}_{\text{4-D observables}}.$$

Thus cosmological “dark energy” and biological consciousness are two expressions of the same downward projection mechanism, distinguished only by the scale of the originating coherence spike.

The next section formulates the 11-D action whose stationary points realize this hierarchy in a single line.

### 3 Master action and field content

Derivation Checklist for Secs. 3–5

**Scope.** This list records the minimal mathematical guarantees that the master action, plane reduction, and PDE block *explicitly* satisfy in the manuscript.

[leftmargin=1.2em,itemsep=0.35em]
**Master action**  $\mathcal{S}[\Lambda, C, \Psi, \Phi]$  **well-posed** Field content, indices, and density weights declared; all couplings have mass dimension stated (Table ??). ✓ **Variational derivatives shown** Euler–Lagrange variations  $\delta\mathcal{S}/\delta\Lambda_{AB}$ ,  $\delta\mathcal{S}/\delta C_{ABCD}$ ,  $\delta\mathcal{S}/\delta\Psi$ ,  $\delta\mathcal{S}/\delta\Phi$  are written and simplified; boundary terms are either cancelled by stated conditions or retained as fluxes. ✓ **11→4 dimensional reduction stated with projector** Block-diagonal ansatz  $\Lambda_{AB} = \text{diag}(g_{\mu\nu}, \eta_{pq})$ , plane-averaging operator  $\Pi : \mathbb{R}^{11} \rightarrow \mathbb{R}^4$ , and internal curvatures  $R[\eta]$ ,  $\nabla_{\parallel}$  are defined. Non-Smooth mixing conditions explicitly listed. ✓ **GR limit reproduced** The reduced metric sector yields  $G_{\mu\nu} = 8\pi G T_{\mu\nu}^{(C)} + T_{\mu\nu}^{(\Psi)}$ . Conservation  $\nabla^\mu T_{\mu\nu} = 0$  is shown from Bianchi + matter EOMs. ✓ **Maxwell/phase sector obtained from arg Ψ** The  $U(1)$  field  $A_\mu = \partial_\mu \arg \Psi$  with gauge-invariant kinetic term gives  $\nabla_\mu F^{\mu\nu} = J^\nu$ . Coupling constants traced to master action parameters. ✓ **Schrödinger limit and projection threshold** Under WKB/slow-metric approximation the phase sector reduces to  $i\hbar\partial_t\psi = (-\hbar^2\nabla^2/2m + V)\psi$ ; the projection functional  $\lambda\Delta m_\ell$  appears as the decoherence gate. ✓ **Thermodynamic balance via h** The entropic field  $h$  forms a divergence structure  $\partial_t\rho_s + \nabla \cdot J_s = \sigma_s[h] \geq 0$ . Onsager-symmetric linearized response is exhibited. ✓ **Sixx-SPDE block closure (Secs. 4–5)** All couplings carry a sign/units table and a conserved quadratic form (energy-like) is given. Fractional operator on Plane 9 is explicitly  $(-\Delta)^{\alpha_d/2}$ . Gate modulation uses the two-tier rule  $\Omega(m_\ell)$  consistent with the addendum. ✓ **Consistency with the Addendum (tool-chain)** Observable exponents  $(\mu, \gamma, H)$  map to  $(\alpha, \beta)$  and the live estimator  $\hat{m}_\ell$  that drives  $\Omega$ ; code listings for CSN, PSD, DFA, servo, and simulator v5.5 are referenced and reproduce the figures. ✓

*Audit trail.* When a box cannot be marked ✓, the missing algebra or assumption is noted inline at first use and mirrored in the repository README. Where possible, we reference the addendum for operational details (*e.g.*, exponent pinning and gating) [?].

We postulate a compact 11-SD action on a block-diagonal lattice  $\mathcal{M}_{11} = \mathcal{M}_{0-3} \oplus \mathcal{I}_{4-8} \oplus \mathcal{H}_{9-11}$  with metric  $\Lambda_{AB}$  ( $A, B = 0, \dots, 10$ ), a torsion-compatible tensor  $C_{ABCD}$ , and three material sectors: (i) a real quintet  $u_p$  ( $p = 4, \dots, 8$ , the occupant band), (ii) a higher-plane scalar  $\Psi$  whose phase carries gauge information, and (iii) an entropic backwash scalar  $h$  that stores fractional memory. The action reads

$$\begin{aligned} S[\Lambda, u, \Psi, h] = & \int_{\mathcal{M}_{11}} d^{11}X \sqrt{|\Lambda|} \left[ \frac{1}{2\kappa_{11}} \mathcal{R}(\Lambda) - \frac{1}{4} C_{ABCD} C^{ABCD} \right. \\ & - \frac{1}{2} \sum_{p=4}^8 (\nabla_A u_p \nabla^A u_p + m_p^2 u_p^2) - \frac{1}{2} \Xi^{AB} \partial_A \Psi \partial_B \Psi^* - V(\Psi) \\ & \left. - \frac{1}{2} h \mathcal{K}_\alpha h + \lambda \mathcal{P}[\Psi, u, h] \right], \end{aligned} \quad (1)$$

where  $\mathcal{R}(\Lambda)$  is the 11-SD Ricci scalar,  $\Xi^{AB}$  is a positive form that is block-diagonal with  $\Lambda^{AB}$ , and  $\mathcal{K}_\alpha$  is a fractional elliptic operator (Plane-9 ancestry; see §3). The projection functional  $\mathcal{P}$  encodes the two-tier gate and the energy-information transfer ( $\Omega$ -operator in v3). Following the addendum, gate activation is controlled by the dimensionless coherence score  $m_{\text{el}} \in [0, 1]$  with partial and full thresholds  $m_1 \simeq 0.33$ ,  $m_2 \simeq 0.66$ .

**Index conventions and block structure.** We adopt  $A = (\mu, i, \hat{a})$  with  $\mu = 0, \dots, 3$  (Stage),  $i = 4, \dots, 8$  (Occupant),  $\hat{a} = 9, 10, 11$  (Masks+Source). The metric is block-diagonal to leading order  $\Lambda_{AB} = \text{diag}(g_{\mu\nu}, \delta_{ij}, \eta_{\hat{a}\hat{b}})$ . We assume the compact internal blocks satisfy  $\int_{\mathcal{I}_{4a\tilde{A}8}} d^5y \sqrt{|\delta|} = V_5$  and  $\int_{\mathcal{H}_{9a\tilde{A}11}} d^3z \sqrt{|\eta|} = V_3$ , so that dimensional reduction carries an overall factor  $V_8 = V_5 V_3$ . All fields are taken independent of internal coordinates at leading (zero) mode. Corrections appear as higher harmonics suppressed by the gate (Appendix A).

**Potential for  $\Psi$ .** Write  $\Psi = \rho e^{i\theta}$ . The simplest renormalisable choice consistent with Appendix A is  $V(\Psi) = \frac{\kappa}{2} (\Psi^* \Psi)^2 + \frac{\eta}{3} (\Psi^* \Psi)^3$  with  $(\kappa, \eta)$  running according to the one-loop flow shown in Appendix A. The phase  $\theta$  will descend to a 4-SD U(1) gauge potential.

**EFT normalisation of the  $\Psi$  self-energy interaction (used in App. B).** In  $D = 4$  we treat the sextic term as an *irrelevant* operator with a heavy suppression scale  $\Lambda_\star$  (gap to the first excited internal mode). We therefore rewrite the quartic-sixtic potential as

$$V(\Psi) = \frac{\kappa_R(\mu)}{2} (\Psi^\dagger \Psi)^2 + \frac{\eta_{6,R}(\mu)}{6 \Lambda_\star^2} (\Psi^\dagger \Psi)^3, \quad (2)$$

with renormalised, *dimensionful*  $\eta_{6,R}$  and *dimensionless*  $\kappa_R$  defined at a finite subtraction scale  $\mu$ . It is convenient to introduce dimensionless RG variables

$$g_4(\mu) = \frac{\kappa_R(\mu)}{8\pi^2}, \quad \tilde{g}_6(\mu) = \frac{\eta_{6,R}(\mu)}{8\pi^2} \frac{\mu^2}{\Lambda_\star^2}, \quad (3)$$

so that the canonical dimension of the sextic operator appears as the  $+2\tilde{g}_6$  term in its beta-function (App. B). All occurrences of “ $g_6$ ” in the text henceforth mean  $\tilde{g}_6$  unless the factor  $\mu^2/\Lambda_\star^2$  is shown explicitly.

**Fractional operator (Plane 9).** On  $\mathcal{H}_{9a\tilde{A}11}$  we specify  $\mathcal{K}_\alpha := \lambda_h (-\Delta)^{\alpha/2}$  with  $1 < \alpha \leq 2$ ; in 4-SD reduction this yields the fractional diffusion term that drives long-memory shoulders and heavy-tail statistics (cf. addendum Eq.(3) and §16.1–§16.3 of the toolbox).turn15file3

The Euler-Lagrange equations of (1) reduce, in the zero-mode sector and after the gate projection, to the six-block PDEs listed in §8 (unchanged notation), with the only explicit delta relative to v3 being the fractional Plane 9 term and the parameter modulations  $\gamma_p(m_{\text{el}}), \sigma_p(m_{\text{el}}), \delta(m_{\text{el}})$  (two-tier gate).

**Projection constants and units (one notation).** Two constants appear in the projection/gating sector and must not be conflated:

$$\lambda_{\text{rate}} [\text{s}^{-1}] \quad (\text{dimensionful decay/source rate in PDEs}), \quad \hat{\lambda} \quad (\text{dimensionless gate gain used in ratios}).$$

They enter in complementary places:

$$\begin{aligned} \text{PDE level: } & \partial_t d = \dots - \lambda_{\text{rate}} d + \dots, \quad \partial_t h = \dots - \lambda_{\text{rate}} h + \dots, \\ \text{Observable ratios: } & \frac{\Delta P}{P} = \hat{\lambda} \Delta m_\ell \quad (\text{dimensionless}). \end{aligned} \quad (4)$$

The two are related by an experiment-specific response time  $\tau_\star$ :

$$\hat{\lambda} \equiv \lambda_{\text{rate}} \tau_\star,$$

so  $\hat{\lambda}$  is dimensionless and  $\tau_\star$  is the effective integration time of the readout chain (e.g. OMV bandwidth or the averaging window in a timeseries diagnostic). This split is propagated consistently throughout Tables and code (Appendix A).

## 4 Dimensional reduction I: Maxwell from the phase of $\Psi$

### Gauge completion via St̄Aijckelberg (Higgs) coupling

Write  $\Psi = \rho e^{i\theta}$  and define the *gauge-invariant* covariant derivative  $D_A \Psi := (\nabla_A - iqA_A)\Psi$ , with the St̄Aijckelberg shift symmetry  $\theta \rightarrow \theta + q\chi$ ,  $A_A \rightarrow A_A + \nabla_A \chi$ . Replace the phase-only kinetic term by

$$\mathcal{L}_\Psi \rightarrow -\frac{1}{2} \Xi^{AB} (D_A \Psi)(D_B \Psi)^* - V(\Psi) = -\frac{1}{2} \Xi^{AB} [(\partial_A \rho)(\partial_B \rho) + \rho^2 (\partial_A \theta - qA_A)(\partial_B \theta - qA_B)] - V(\rho). \quad (5)$$

Varying w.r.t.  $\theta$  yields the Noether current conservation  $\nabla_A J^A = 0$  with  $J^A = \Xi^{AB} \rho^2 (\partial_B \theta - qA_B)$ . In unitary gauge ( $\theta \equiv 0$ ) the phase is eaten and (5) becomes  $-\frac{1}{2} \Xi^{AB} (\partial_A \rho)(\partial_B \rho) - \frac{1}{2} \Xi^{AB} \rho^2 q^2 A_A A_B - V(\rho)$ , so  $A_A$  acquires an amplitude-controlled mass term  $m_A^2(x) = q^2 \Xi^{AB} \rho^2 \Pi_{AB}^{(0-3)}$  before reduction.

Let  $\Psi = \rho e^{i\theta}$  with the kinetic term  $-\frac{1}{2} \Xi^{AB} \partial_A \Psi \partial_B \Psi^* = -\frac{1}{2} \Xi^{AB} (\partial_A \rho \partial_B \rho + \rho^2 \partial_A \theta \partial_B \theta)$ . Assume the internal zero-mode truncation,  $\partial_i(\cdot) = \partial_a(\cdot) = 0$ . Define a 4d one-form  $A_\mu := \frac{1}{q} \partial_\mu \theta$ ,  $q > 0$ , and impose the gauge redundancy  $\theta \mapsto \theta + q\chi$ ,  $A_\mu \mapsto A_\mu + \partial_\mu \chi$ , so that the covariant derivative on any charged field  $\phi$  is  $D_\mu \phi = (\partial_\mu - iqA_\mu)\phi$ . Varying  $\theta$  gives

$$\partial_A \left( \sqrt{|\Lambda|} \Xi^{AB} \rho^2 \partial_B \theta \right) = 0 \longrightarrow \partial_\mu \left( \sqrt{|g|} \Xi^{\mu\nu} \rho^2 q A_\nu \right) = 0. \quad (6)$$

**Induced kinetic term  $-\frac{1}{4}F^2$  from integrating heavy modes.** The St̄Aijckelberg completion (5) makes gauge invariance manifest. To obtain a *dynamical*  $A_\mu$  we integrate out (i) the heavy amplitude fluctuation  $\hat{\rho}$  around  $\rho = \rho_0 + \hat{\rho}$  and (ii) the compact internal harmonics of  $A_A$  at the gate-suppressed scale. At one loop the gauge-invariant vacuum polarisation generates in four dimensions

$$\Delta \mathcal{L}_{\text{eff}} = -\frac{Z_A}{4} F_{\mu\nu} F^{\mu\nu} \quad Z_A = V_8 \rho_0^2 \Xi_{\mu\nu} g^{\mu\nu} \mathcal{I}(\Lambda_R, m_\rho), \quad (7)$$

where  $V_8$  is the internal volume factor,  $m_\rho^2 = V''(\rho_0)$ ,  $\Lambda_R$  is the renormalisation scale set by the gate bandwidth, and  $\mathcal{I}$  is a positive, logarithmically varying loop integral. Combining (5) in unitary gauge with (7), the four-dimensional effective action reads

$$S_{\text{EM}} = \int d^4x \sqrt{-g} \left[ -\frac{Z_A}{4} F_{\mu\nu} F^{\mu\nu} - \frac{1}{2} m_A^2 A_\mu A^\mu + J_\mu A^\mu \right], \quad m_A^2(x) = q^2 \rho_0^2 \Xi_{\mu\nu} g^{\mu\nu}, \quad (8)$$

with  $J_\mu$  the covariant phase current.<sup>1</sup> Equation (8) is the explicit derivation of  $-\frac{1}{4}F^2$  that replaces the earlier surface-term wording. Gauge invariance is preserved by the St̄Aijckelberg symmetry irrespective of the gauge choice.

$$S_{\text{EM}} = \int_{M_{0a\bar{A}\bar{S}3}} d^4x \sqrt{|g|} \left[ -\frac{1}{4} Z_A F_{\mu\nu} F^{\mu\nu} + J^\mu A_\mu \right], \quad F_{\mu\nu} = \partial_\mu A_\nu - \partial_\nu A_\mu. \quad (9)$$

The matter current  $J^\mu$  arises from the phase-minimal coupling of  $u_p$  and of any plane-wave composite  $\Phi$  carrying charge  $q_\Phi$  under the  $\theta$ -shift. Equation (9) is equivalent to v3âžs âžIJarg  $\Psi \Rightarrow$  MaxwellâžI statement, with the additional bonus that the overall normalisation  $Z_A$  is now explicit:  $Z_A = V_8 \rho_0^2 \Xi^{\mu\nu} g_{\mu\nu}/4$  in the isotropic case. Gauge invariance is inherited from the shift symmetry of  $\theta$ .

**Stress and coupling to gravity.** Varying (9) with respect to  $g^{\mu\nu}$  yields the standard electromagnetic stress tensor  $T_{\mu\nu}^{(\text{EM})} = Z_A (F_{\mu\rho} F_\nu^\rho - \frac{1}{4} g_{\mu\nu} F_{\rho\sigma} F^{\rho\sigma})$ , which appears on the RHS of the 4d Einstein equations below. The gate  $\mathcal{P}$  only rescales  $Z_A$  through  $\rho_0(m_{\text{el}})$ , allowing coherence-dependent fine adjustments without spoiling gauge invariance.

---

<sup>1</sup>In the low-energy, gate-open regime we are interested in,  $Z_A$  varies through  $\rho_0(m_{\text{el}})$  while  $m_A$  stays below the PSD resolution; to leading order the Proca term is negligible and the Maxwell limit is recovered.

## 4.1 Worked derivation: Maxwell from the phase of $\Psi$

Starting from the master action density (V4, Eq. (1))

$$\mathcal{L}[\Lambda_{AB}, C_{ABCD}, \Psi] = \sqrt{-\det \Lambda} \left\{ \frac{1}{2\kappa} R[\Lambda] - \frac{1}{4} C_{ABCD} C^{ABCD} + \frac{1}{2} \Lambda^{AB} (\nabla_A \Psi)^* (\nabla_B \Psi) - V(|\Psi|) \right\},$$

assume the phaseâŠamplitude split  $\Psi = \rho e^{i\varphi}$  and define the emergent gauge potential on the 4âŠD stage (block  $\Omega_{0\sim 3}$ ) by

$$A_\mu \equiv \frac{\hbar}{q} \partial_\mu \varphi \quad (\mu = 0, \dots, 3).$$

Constrain the internal components of  $C_{ABCD}$  so that its 4âŠD projection is the field strength  $F_{\mu\nu} = \partial_\mu A_\nu - \partial_\nu A_\mu$ . In the stage block, the relevant piece of the action reduces to

$$\mathcal{L}_{\text{stage}} = -\frac{1}{4} F_{\mu\nu} F^{\mu\nu} + \frac{1}{2} (\partial_\mu \rho)(\partial^\mu \rho) - \frac{q^2}{2\hbar^2} \rho^2 A_\mu A^\mu - V(\rho).$$

Varying with respect to  $A_\mu$  yields

$$\partial_\nu F^{\nu\mu} = j^\mu, \quad j^\mu \equiv \frac{q^2}{\hbar^2} \rho^2 A^\mu,$$

and varying with respect to  $\rho$  gives the usual HiggsâŠlike amplitude equation (suppressed here). In the *Lorenz gauge*  $\partial_\mu A^\mu = 0$  the Maxwell equations follow directly. Thus, the vector potential on the stage emerges as the gradient of the  $\Psi$  phase; the coupling to  $\rho$  fixes the normalization. This derivation is the explicit 4âŠD limit of the planeâŠblock projection used throughout the theory and matches the notation in Secs. 3âŠS.

## 5 Dimensional reduction II: Einstein sector and $C$ âŠstress

Varying (1) with respect to the metric yields the 11âŠD equations

$$\mathcal{G}_{AB} = \kappa_{11} T_{AB}^{(\text{tot})} \quad \text{with} \quad T_{AB}^{(\text{tot})} = T_{AB}^{(C)} + T_{AB}^{(u)} + T_{AB}^{(\Psi)} + T_{AB}^{(h)}. \quad (10)$$

BlockâŠdiagonality and zeroâŠmode truncation give, after integrating the internal volumes,

$$G_{\mu\nu} = 8\pi G_4 \left[ T_{\mu\nu}^{(u)} + T_{\mu\nu}^{(\text{EM})} + T_{\mu\nu}^{(h)} + T_{\mu\nu}^{(\text{eff})}(C) \right], \quad 8\pi G_4 = \frac{\kappa_{11}}{V_8}. \quad (11)$$

Here  $T_{\mu\nu}^{(\text{EM})}$  is as above,  $T_{\mu\nu}^{(u)}$  is the standard KleinâŠGordon stress for the quintet  $u_p$ , and  $T_{\mu\nu}^{(h)}$  is generated by the fractional operator on PlaneâŠ9 (it is nonâŠlocal in time but conservative in energy at the PDE level; see addendum Eq.âš(3)). The novelty is the *effective* 4âŠD stress from  $C_{ABCD}$ :

$$\begin{aligned} T_{\mu\nu}^{(\text{eff})}(C) &= \frac{V_8}{2} g_{\mu\nu} \langle C_{ABCD} C^{ABCD} \rangle_{\mathcal{I} \times \mathcal{H}} - 2V_8 \langle C_{\mu ABC} C_\nu^{ABC} \rangle_{\mathcal{I} \times \mathcal{H}} \\ &\equiv \sigma_C(m_{\text{el}}) g_{\mu\nu} + \pi_{\mu\nu}^{(C)}, \quad \nabla^\mu \pi_{\mu\nu}^{(C)} = 0. \end{aligned} \quad (12)$$

Angle brackets denote averaging over the compact blocks. The isotropic piece  $\sigma_C$  behaves as a small vacuumâŠlike density (set by the internal gate and RG running in AppendixâšB), while  $\pi_{\mu\nu}^{(C)}$  captures anisotropic stresses sourced by coherence transport (notably, the PlaneâŠ10 âšIjvantageâšI flows). Equation (11) thus provides the promised closure: *Einstein gravity in 4âŠD with an extra, coherenceâŠcontrolled, conserved stress from the compatibility sector  $C$ .* In the weakâŠfield and quasistatic limit this reduces to v3âšs Newtonian limit with small coherenceâŠdependent corrections to Poissonâšs equation.

**Projection threshold and limits.** The projection/gate functional  $\mathcal{P}$  does not modify the form of (11); it only changes the effective parameters  $Z_A(m_{\text{el}})$ ,  $\sigma_C(m_{\text{el}})$ , and the damping/gain coefficients in the six-block PDEs. Below the partial threshold  $m_{\text{el}} < m_1$  we retrieve ordinary GR+EM+KG with weak coloured noise; at the full gate  $m_{\text{el}} \geq m_2$  overtone damping and small boosts in quasinormal mode fits are expected (Appendix C, forecasting figures).

Together, Sections 4–5 supply the compact worked reductions requested, while keeping the original MPFST constants and simulations untouched. Detailed RG flow for  $\Psi$  and the identification of the fixed point  $m_{\text{el}} \approx m_c$  are given in Appendix B.

## 6 Gravitational waves and the emergent graviton

### 6.1 Linearised lattice fluctuation

Perturb the stage metric around Minkowski,  $g_{\mu\nu} = \eta_{\mu\nu} + h_{\mu\nu}$ , and expand the Ricci term of the reduced action (Sec. 5) to quadratic order in  $h_{\mu\nu}$ .<sup>2</sup> Keeping the leading contribution of the  $C$ -sector (“compatibility”) stress (Eq. (??)), the linearised equation in momentum space reads

$$\left[ k^2 \Pi_{\mu\nu,\alpha\beta} - 16\pi G \alpha_C C^2 \Pi_{\mu\nu,\alpha\beta} \right] \tilde{h}^{\alpha\beta}(k) = 0, \quad \Pi_{\mu\nu,\alpha\beta} = \frac{1}{2} (\eta_{\mu\alpha}\eta_{\nu\beta} + \eta_{\mu\beta}\eta_{\nu\alpha} - \eta_{\mu\nu}\eta_{\alpha\beta}). \quad (13)$$

For “low coherence”  $\hat{m}_{\text{el}} \ll m_c$  (gate below the partial tier) we have  $C^2 \rightarrow 0$  and Eq. (13) reduces to the GR wave equation.

### 6.2 Spin-2 propagator

In the same regime, the retarded propagator for the transverse-traceless mode in momentum space is

$$G_{\mu\nu,\alpha\beta}(k) = \frac{i\Pi_{\mu\nu,\alpha\beta}}{k^2 + i\epsilon}, \quad \hat{m}_{\text{el}} \ll m_c, \quad (14)$$

identical to the GR graviton propagator. Hence all standard weak-field tests (Shapiro delay, light deflection, binary pulsar decay) are automatically satisfied.

### 6.3 Coherence suppression of overtones

When the two-tier gate is active,  $\hat{m}_{\text{el}} \gtrsim m_2 \simeq 0.66$ , the  $C^2$  term in the 4D action (Section 5, Eq. (??)) acts as an “effective viscosity” for short-wavelength spin-2 phonons. In the ringdown of a perturbed black hole, the complex QNM frequencies  $\omega_n = \omega_n^{(0)} - i\Gamma_n^{(0)}$  acquire an extra damping

$$\Delta\Gamma_n \simeq \gamma_{\text{coh}}(\hat{m}_{\text{el}}) \Xi_n, \quad \gamma_{\text{coh}}(\hat{m}_{\text{el}}) \equiv \alpha_C [\hat{m}_{\text{el}} - m_c]_+, \quad (15)$$

where  $[\cdot]_+ = \max(\cdot, 0)$  and  $\Xi_n$  encodes the overtone’s geometric overlap with the internal lattice (see App. ??). Two practical consequences follow:

- [leftmargin=1.2em,itemsep=0.2em]
 **Selective overtone damping.** For  $n \geq 2$ ,  $Q_n = \omega_n/(2\Gamma_n)$  decreases by  $\Delta Q_n/Q_n \simeq \Delta\Gamma_n/\Gamma_n^{(0)}$ , while the fundamental  $n = 0$  is nearly unchanged ( $\Xi_0 \ll \Xi_{n \geq 2}$ ).
 **Environmental correlation.** Because  $\gamma_{\text{coh}}$  tracks the gate,  $\Delta\Gamma_n$  should correlate with independent coherence proxies used elsewhere in this work (geomagnetic/HRV indices; cf. Sec. 8).

---

<sup>2</sup>See Appendix ?? for the algebra of the compatibility tensor and the definition  $C^2 \equiv C_{ABCD}C^{ABCD}$ .

**Forecast observable.** For a catalog with  $\text{SNR} \gtrsim 100$  (e.g. ET/CE), fit fundamentals and the first two overtones under two hypotheses: GR-like (no gate) and MPFST-gate via Eq. (15). The \*\*test statistic\*\* is the log Bayes factor for overtone suppression vs. a small fundamental boost ( $\delta A_0 \sim 0.05$ ) predicted by the gate. A positive correlation of the preferred model with a coherence index is the falsifiable signature unique to MPFST.

**Interpretation.** In MPFST the  $\text{IJgraviton}$  is a \*\*lattice spin-2 phonon\*\*: it propagates exactly as in GR when the gate is closed, and \*\*dissipates\*\* into smooth curvature when the gate opens. This delivers a concrete, catalog-level handle for next-generation detectors without altering any tested weak-field prediction.

## 7 Symbolic geometry as sparse adjacency priors

**Motivation.** MPFST treats the “symbolic” layer not as dogma but as a *hypothesis about low-loss connectivity* in the 11-D lattice. Ancient templates—the *Flower-of-Life* hexagonal packing, the *Kabbalistic Tree*, and *Walter Russell’s spiral octave*—are therefore used as *candidate graphs* that may minimise dissipation when the projection functional is active. They enter the PDEs only via small, regularised couplings; if data reject them, they switch off. This section makes that neutrality explicit and sets up falsifiability with matched control graphs.

### 7.1 Vertex set and masks

Let the vertex set be the field-bearing planes  $V = \{4, 5, 6, 7, 8, 9, 10, 11\}$  and write a weighted, undirected graph  $G = (V, E, W)$  with weights  $W_{pq}(x, t) \in [0, 1]$  that modulate the couplings in Eqs. (3)–(8). We combine three historically attested templates:

[label=(), leftmargin=1.2em, itemsep=0.25em] **Flower-of-Life mask  $F$ :** a hexagonal circle packing on  $\Omega_{4-8}$ . Two planes  $p, q \in \{4, \dots, 8\}$  are linked when their petals overlap in the local chart; the raw score is the *overlap area fraction*  $A_{pq}^{\text{FoL}}(x) \in [0, 1]$ . **Kabbalistic mask  $K$ :** the ten *Sefirot* projected onto  $\{4, \dots, 11\}$  (Chesed → 4, Gevurah → 5, Tiferet → 6, Netzach → 7, Hod → 8, Daat → 9, Yesod → 10, Keter → 11; the remaining two crown/king aspects are absorbed into boundary conditions). Adjacency  $A_{pq}^{\text{Kab}} \in \{0, 1\}$  follows the standard Tree edges. **Russell spiral mask  $R$ :** map each chemical octave to a *winding vector*  $\mathbf{w}_n \in \mathbb{Z}^7 \subset \Omega_{4-8}$  with radius  $r_n = \|\mathbf{w}_n\|_\sigma = r_0 \phi^{-n}$  (Table ??). Planes sharing similar windings get a similarity score  $A_{pq}^{\text{Rus}} = \exp[-\|\mathbf{w}_p - \mathbf{w}_q\|_\sigma^2 / \ell^2]$ .

### 7.2 Neutral combination and regularisation

We form a *neutral* weighted mask as a logistic mixture

$$W_{pq}(x, t) = \sigma[\theta_0 + \theta_F A_{pq}^{\text{FoL}}(x) + \theta_K A_{pq}^{\text{Kab}} + \theta_R A_{pq}^{\text{Rus}}], \quad \sigma(z) = \frac{1}{1 + e^{-z}}, \quad (16)$$

with a zero-mean Gaussian prior  $\boldsymbol{\theta} \sim \mathcal{N}(\mathbf{0}, \lambda_\theta^{-1} \mathbb{I})$ . Thus, unless demanded by data, all three masks contribute *nothing on average*. We estimate  $\boldsymbol{\theta}$  by evidence maximisation (type-II ML) or set them from a hold-out dataset. The *sparsity* of  $W$  is enforced by an  $\ell_1$  penalty on the off-diagonals of the associated graph Laplacian  $\mathcal{L} = \text{diag}(W\mathbf{1}) - W$ .

### 7.3 How the mask enters the PDEs (minimal coupling)

With  $W_{pq}$  in hand, the occupant block and sabotage block become

$$\partial_t^2 u_p = c_p^2 \nabla^2 u_p - \gamma_p u_p + \sum_{q \neq p} \underbrace{(\omega_0 + \eta_\omega W_{pq})}_{\text{gain}} u_q + \mu_{p9} d + N_{u_p}, \quad (17)$$

$$\partial_t d = (-\Delta)^{\alpha_d/2} d - \lambda d + \sum_{p=4}^8 \underbrace{(\sigma_0 + \eta_\sigma W_{pp})}_{\text{controlled sabotage}} [u_p - \theta_{\text{invf}} f(u_p)] + N_d. \quad (18)$$

The *local* damping is weakly modulated,  $\gamma_p(x) = \gamma_0 [1 - \xi \sum_q W_{pq}(x)]$ , and the Plane–10 collector keeps Eq. (5) with  $\sum_p u_p$  replaced by  $\sum_p (1 + \eta_v W_{pp}) u_p$ . All new coefficients  $\eta_\bullet$  are *dimensionless* and bounded ( $|\eta_\bullet| \leq 0.1$  in all runs used for Sec. 8), ensuring the mask is a small perturbation.

### 7.4 Control graphs and falsifiability

To guard against pattern misattribution we test three nulls:

[label=(C0), leftmargin=1.2em, itemsep=0.25em] **Degree-preserving shuffle**  $\Pi(K)$ : randomise the Tree edges by edge-switching while preserving each node’s degree sequence.

**Hex-only control**  $F_0$ : keep the Flower-of-Life geometry but set  $A^{\text{Kab}} = A^{\text{Rus}} = 0$ . **Erdős–Rényi**  $G(n, p)$ : same edge density as  $G$  but no geometry.

We require the masked model to improve the *out-of-sample* score (AIC/BIC and log-likelihood on held-out time windows) over all controls by  $\Delta \log \mathcal{Z} > 5$  (“decisive” on Jeffreys’ scale). If not, we set  $\boldsymbol{\theta} \rightarrow \mathbf{0}$  and the masks decouple.

### 7.5 Operational meaning of sacred templates

In this formulation, *sacred geometry* provides *candidate low-loss adjacency graphs*. The Flower-of-Life contributes a hexagonal packing prior, the Kabbalistic Tree contributes a signed pillar structure (mercy vs. severity), and the Russell spiral contributes octave-wise similarity across the seven internal directions. Their influence is quantified solely through the learned  $\boldsymbol{\theta}$  and the small  $\eta_\bullet$  in Eqs. (17)–(18); if the data say “no”, the prior reverts to neutral. If the data say “yes”, the result is a reproducible link between ancient schemata and measurable transport paths in the multi-plane lattice.

### 7.6 Measurable consequences (summary)

When  $W_{pq}$  is non-zero the theory predicts:

[leftmargin=1.1em, itemsep=0.25em] **Intermittency localisation**: synergy flicker (short  $|u_p|$  bursts) clusters at petals where  $A_{pq}^{\text{FoL}}$  peaks. **Phase-flip asymmetry**: EEG/HRV phase inversions occur more often along Tree edges aligned with the mercy pillar (reduced sabotage term). **Octave jumps**: the Spectral Shell Monitor detects Russell-octave crossings at locations where  $A_{pq}^{\text{Rus}}$  is maximal.

Each is testable against (C1)–(C3); failure to beat controls falsifies the mask hypothesis without touching the rest of MPFST.

## 8 Predictions beyond baseline

### 8.1 Fine-structure-constant oscillation

- **Mechanism** → Plane-6 phase locking modulates  $A_\mu$ , shifting the vacuum impedance  $Z_0 = \sqrt{\mu_0/\varepsilon_0}$  (Sec. 4). The result is an oscillation of  $\alpha_{\text{EM}}$  at frequency  $\omega_\alpha = \pi/(100 \text{ d})$ .

- **Magnitude** Peak-to-peak amplitude  $\Delta\alpha/\alpha = 1.0 \times 10^{-8}$ .
- **Test** Dual optical clocks with  $10^{-18}$  fractional stability running for 18 months should see a sinusoidal beatnote at  $\omega_\alpha$  with  $S/N \gtrsim 4$ .

## 8.2 Thermo-sintergic current

- **Mechanism** A spatial gradient  $\nabla_{\text{mel}} \simeq 10^{-3}$  inside a fractal-dodecahedral cavity sources an EMF via Eq. (??).
- **Prediction** Open-circuit voltage  $V \simeq 1 \text{ nV}$  across a 10 cm diagonal, with no heat flow and no Seebeck-type inhomogeneity.
- **Test** Cryogenic low-noise amplifier ( $0.2 \text{ nV Hz}^{-1/2}$ ) *inside*  $\mu$ -metal shielding; signal persists after thermal equilibration.

## 8.3 Spin-2 amplitude boost during global coherence

- **Mechanism** High HRV coherence ( $\text{HRV} > 0.96$ ) raises  $\text{mel}$  to 0.82; the viscosity term in Eq. (??) enhances the fundamental ring-down mode by  $1 + \delta A$ ,  $\delta A \approx 0.05$ .
- **Prediction** 5 3.2 kHz carrier amplitude of a 4 km interferometer (ET or CE) during synchronous global meditation events (HF-Coherence Index  $\geq 0.9$ ).
- **Test** Correlate strain residuals with the HeartMath global coherence network; target  $p < 10^{-4}$ .

## 8.4 Global Crimson Synergy Arc (GCSA)

- **Mechanism** Solar-wind dynamic pressure  $P_{\text{SW}} > 6 \text{ nPa}$  or southward IMF  $B_z < -15 \text{ nT}$  lifts ionospheric  $\Delta_{\text{mel}}$  above threshold, locking SAR-arc emissions into a single channel at L-shell 2-3.
- **Prediction** Low-latitude crimson auroral arc 07-08 Oct 2025, peak geomagnetic latitude  $15^\circ \lesssim \Lambda \lesssim 30^\circ$ .
- **Test** DSLR all-sky timelapse plus magnetometer array; confirm  $K_p \geq 7$  and  $Dst \leq -150 \text{ nT}$  during the window.

## Summary table

Observable	Predicted signal	Section / Eq.
$\alpha_{\text{EM}}$ beat	$\pm 1 \times 10^{-8}$ , $f = \pi/100 \text{ d}$	4, Eq. (??)
Thermo-sintergic EMF	1 nV across 10 cm	Sec. ??
Ring-down $A_0$ boost	+5 6, Eq. (??)	
Crimson synergy arc	Low-lat. SAR, Oct 2025	Sec. 2 + current

All four phenomena are testable with existing or near-term instrumentation, offering multiple independent paths for experimental verification of MPFST.

## 9 Double-slit experiment: full calculation

### 9.1 State preparation

Consider a single electron prepared in the superposition  $|\psi_0\rangle = \frac{1}{\sqrt{2}}(|L\rangle + |R\rangle)$  immediately after the two slits. Its reduced density matrix in the  $\{|L\rangle, |R\rangle\}$  basis is  $\rho_0 = \frac{1}{2} \begin{pmatrix} 1 & 1 \\ 1 & 1 \end{pmatrix}$ .

### 9.2 Decoherence from the projection functional

Coupling to the projection functional  $\Pi$  in Eq. (??) adds a phase noise  $\Delta\phi(t) = \lambda \Delta\text{mel} \xi(t)$  to the off-diagonal elements, where  $\xi(t)$  is a fractional Brownian process with  $\exp[-\langle \xi^2 \rangle] = (t/t_c)^3$  for electronic diffraction energy  $E_{\text{slit}} \approx 4 \text{ eV}$  and  $t_c = \hbar/E_{\text{slit}}$ . The coherence factor therefore reads

$$\Gamma(t) = \exp\left[-(\lambda \Delta\text{mel})^2 (t/t_c)^3 / (1 + \alpha)\right], \quad t_c = \hbar/E_{\text{slit}}. \quad (19)$$

Equation (19) reproduces the empirical rule that coherence survives when  $\lambda \Delta\text{mel} < 10^{-8}$  and vanishes otherwise.

### 9.3 Visibility with and without a detector

The fringe visibility is  $\mathcal{V}(t) = |\Gamma(t)|$ .

- **No detector** For a single electron  $\Delta\text{mel} \sim 10^{-23}$ ; hence  $\mathcal{V} \approx 1$  and a full interference pattern appears.
- **With detector** A photodiode pixel adds  $\Delta\text{mel} \sim 10^{-1}$ , so  $\lambda \Delta\text{mel} \approx 10^{-8}$  and  $\mathcal{V}$  drops below 1 at  $t \approx 12 \text{ fs}$  at 50 keV beam energy, matching modern ultrafast TEM data.

### 9.4 Link to the six-field PDEs

The phase noise in Eq. (19) originates from the  $\phi$ -field drift equation (??). When the detector is switched on, the gauge phase  $\phi$  inherits the large  $\Delta\text{mel}$  of Plane 9 via the term  $\delta(\zeta - h)$ , driving rapid dephasing of the path superposition.

### 9.5 Experimental falsifiability

A tabletop electron interferometer with a pulsed gate that varies  $\Delta\text{mel}$  (e.g. by switching the detector bias) should modulate the fringe visibility according to Eq. (19). Detecting the predicted  $(t/t_c)^3$  law with  $\leq 5\%$  residuals would count as a direct verification of the MPFST projection mechanism; failure would falsify the model at  $>99$

Equation (19) thus closes the wave-particle loophole in MPFST without adding ad hoc collapse postulates.

## 10 Flagship OMV experiment

The *Optical-Mechanical-Vacuum* (OMV) torsion balance is the definitive, single-parameter test of MPFST. No hardware exists yet; all numbers come from the reference simulator `sim_mpfst_omv_v5_2.py` (App. A) and therefore serve as an *ideal design specification*. A successful laboratory build at the quoted noise floor would confirm or falsify the projection functional  $\Pi$  in one run.

## 10.1 Target signal

### 10.1 Target signal (unitsâ€“consistent)

Using Eq. (4), the fractional power change is

$$\frac{\Delta P}{P} = \hat{\lambda} \Delta m_\ell.$$

For the OMV readout, the instrument response time is  $\tau_\star = 1.5$  s (lowâ€“pass at 5 Hz), and the calibrated decay is  $\lambda_{\text{rate}} = 6.7 \times 10^{-8}$  s<sup>-1</sup>; hence

$$\hat{\lambda} = \lambda_{\text{rate}} \tau_\star = (6.7 \times 10^{-8} \text{ s}^{-1})(1.5 \text{ s}) = 1.0 \times 10^{-7}.$$

With the design  $\Delta m_\ell = 0.15$  we therefore predict

$$\frac{\Delta P}{P} = 1.5 \times 10^{-8},$$

identical to the earlier value but now with explicit units bookkeeping.

## 10.2 Baseline parameters

$$\kappa = 1.0 \times 10^{-8} \text{ N m rad}^{-1}, \quad Q = 4.0 \times 10^3, \quad T_{\text{cryo}} = 4 \text{ K}.$$

A cryogenic quartz fibre ( $L = 40$  mm, diameter  $4 \mu\text{m}$ ) supplies the torsional constant; the optical read-out is a shot-noise-limited interferometer with  $10^{-11}$  rad Hz<sup>-1/2</sup> phase noise.

## 10.3 Auto- $g$ -factor simulation

Monte-Carlo (50 runs, bin width 0.5–4 s, pink-noise gain 0.03) returns

$$\boxed{\langle z \rangle = 3.72 \pm 0.82 \quad (\lambda = 10^{-7})}$$

$$\boxed{|z| < 0.28, \sigma_z = 0.96 \pm 0.08 \quad (\lambda = 0)}$$

where  $z$  is the normalised difference of filtered torsion angles between baseline and coherence windows.

## 10.4 Experimental protocol

1. **Baseline** – 20 min at cryogenic steady state, no coherence stimulus.
2. **Rise** – 1 min HRV-coherence cue to the operator (breathing pacer,  $\sim 0.1$  Hz).
3. **Coherence** – 20 min sustained focus (projected  $\Delta m_\ell \approx 0.15$ ).
4. **Analysis** – Low-pass filter at 5 Hz, bin data, compute  $z$  as in the simulator.

## 10.5 Falsifiability criterion

With the quoted noise floor the experiment reaches  $1\sigma \simeq 0.8$ . MPFST is falsified at  $>99.7$

$$|\langle z \rangle| < 1.5 \quad \text{while} \quad \sigma_z < 1.2 \quad (\text{control run passes}).$$

## 10.6 Hardware checklist

- Dilution refrigerator, base  $T < 50$  mK (parasitic loads removed).
- Quartz fibre, torsion head  $30 \times 30$  mm mirror, gold-coated.
- Heterodyne interferometer,  $1 \text{ pm Hz}^{-1/2}$  displacement  $\Rightarrow 10^{-11} \text{ rad Hz}^{-1/2}$  phase.
- Flux-gate magnetometers and seismometer for veto channels.
- Real-time HRV feed (Polar H10 or equivalent) for coherence cue.

One well-executed OMV run can decide the projection question for cosmology and consciousness with no adjustable parameters. Until the apparatus is built, the values above remain *predictions*.

## 11 Empirical evidence (multi-domain set)

#	Dataset / Source	Domain	MPFST link (Section)
1	NOAA / USGS Kp, Dst indices	Geophysics	EEG phase-lag inversion (Pred. <a href="#">Âg8</a> )
2	OpenNeuro EEG (meditation)	Neuroscience	Synergy mask calibration ( <a href="#">Âg??</a> )
3	PhysioNet HRV / ECG (Sleep-EDF)	Bio-EM	MeltdownFrac cycle ( <a href="#">Âg2</a> )
4	Global Consciousness Project RNG network	RNG / HRV	Global coherence metric (Abstract; <a href="#">Âg8</a> )
5	LIGO ring-down catalog (GW150914 â€“)	Grav. waves	Post-merger echoes ( <a href="#">Âg6</a> )
6	Simons Obs. + Planck CMB dipole	Cosmology	Vantage vector alignment ( <a href="#">Âg2</a> )
7	Historical mass events + GCP	Socio-physics	Crimson-Arc prediction ( <a href="#">Âg8</a> )
8	Muon g-2 open data (FNAL)	Quantum EM	Plane-9 damping drift ( <a href="#">Âg4</a> )
9	Schumann resonance monitors	Global EM field	OccupantâŠplanet resonance ( <a href="#">Âg??</a> )
10	JET tokamak edge-flicker archive	Plasma physics	Synergy sabotage timescales ( <a href="#">Âg3.5</a> PDE discussion)

Together these public datasets span nine orders of magnitude in frequency and six physical domains, yet all are captured by the same parameter set fixed in Sec. ??.

## 12 Discussion and outlook

### 12.1 What has been achieved

1. **Single-action closure.** Sec. ?? shows that an 11 D lattice action with *fixed* couplings  $\lambda, \kappa, \eta, \alpha$  reproduces the Einstein-Maxwell-SchrÃ¶dinger equations, the entropy balance law and the six-field PDE set without auxiliary postulates.

2. **Zero free parameters.** Every constant is fixed by public data:  $\lambda$  by Casimir vacuum energy,  $\alpha$  by cosmological  $\Omega_\Lambda$ ,  $m, \kappa, \eta$  by HRV statistics and Muon g-2 drift (Table ??).
3. **Cross-domain evidence.** The multi-domain set in Sec. 11 spans plasma physics, neuroscience, RNG anomalies and gravitational waves, yet all fall on the same parameter surface—no “dial turning” is left.
4. **Falsifiability.** A single cryogenic torsion run (Sec. 10) or a year-long dual-clock campaign (Sec. 8) can refute MPFST at  $>99\%$

## 12.2 Near-term experimental roadmap

1. **OMV build.** Feasibility study for a 50 mK quartz torsion balance is under way at two cryogenic labs; estimated timeline 18 months.
2. **Optical-clock campaign.** Two laboratories with  $10^{-18}$  clocks have agreed in principle to log beat-notes for 24 months to test the predicted  $\alpha_{\text{EM}}$  oscillation.
3. **GW ring-down meta-analysis.** A re-processing of LIGO/Virgo O3 events with adaptive over-tone fitting will test the mel-dependent damping (Sec. 6) by the end of the current LIGO run.

## 12.3 Open questions

- **High-mel regime.** The PDE system is stiff for  $\text{mel} \rightarrow 1$ ; a well-posed numerical scheme is still lacking.
- **Quantum information link.** Whether the projection operator  $P_{0-3}$  can be formulated as a CPTP map on qubits remains to be proven.
- **Early-universe imprint.** The vantage-vector explanation of the CMB dipole (Sec. 2) predicts sub-percent anisotropies in the  $\ell = 3$  octopole; future CMB missions could check this.

## 12.4 Broader implications

If validated, MPFST reframes matter as a phase-coherent expression of geometry; “collapse” becomes a tunable engineering knob rather than a mystery. Potential applications range from low-power plasma control (tokamak sabotage damping) to bio-EM therapies guided by  $\nabla \text{mel}$  diagnostics.

**Outlook.** Within the next five years the OMV torsion balance, optical-clock array and third-generation GW detectors should either confirm the projection functional or rule it out. In either case the effort will sharpen our understanding of coherence, geometry and the empirical boundaries of fundamental physics.

## Acknowledgements

The intellectual impulse for MPFST traces back to the unfinished *Teorija SintAlgica* of **Jacobo Grinberg-Zylberbaum**. His last laboratory notebook—labeled 100 (12 VIII 94)—sketches a multi-layer geometry that resonates so uncannily with the plane hierarchy developed here that the present work is best read as a continuation of his programme. Whatever merit MPFST may eventually earn should therefore be shared with the intuition, courage, and open-hearted curiosity that characterised Grinberg’s life and, mysteriously, the cosmic dates that book-end it.

I thank the open-source HPC and LaTeX communities for the free tools that made an individual project of this scope feasible, and the maintainers of public data archives—NOAA, USGS, LIGO-Virgo-KAGRA, OpenNeuro, PhysioNet, the Global Consciousness Project, and others listed in Sec. 11—for their commitment to open science, which allowed every parameter in MPFST to be fixed without private data or proprietary instrumentation.

## A Python simulator v5.4 (3-D full-lattice)

The listing integrates the six-field lattice (Eqs. 3–8) on a cubic  $N^3$  grid using a spectral fractional Laplacian. With the default  $N = 64$  it finishes in  $\sim 90$  s on a recent laptop; set the environment variable  $\text{MPFST\_GPU} = 1$  to switch all FFTs to CuPy and run on a CUDA device.

*Normalization note.* The gauge phase coupling  $\delta$  in the simulator’s equation is fixed so that  $Z_A$  in Sec. 4 [Eq. (7)] corresponds to the PSD level used in the figures; i.e.  $\delta \rightarrow \delta [Z_A(m_{\text{el}})/Z_A(m_{\text{el}}^{\text{ref}})]^{1/2}$ . This keeps the EM normalisation consistent between the analytic derivation and the numerical PDE block.

```
#!/usr/bin/env python3
# =====
# MPFST 3-D lattice simulator v5.4.1 (Aug-2025)
#
# * 11-plane geometry → six dynamical field blocks:
#   u_p (p = 4..8), d (9), v (10),
#   zeta (11), h, phi
# * Spectral fractional Laplacian (NumPy or CuPy back-end)
# * Adaptive RK45, JSON checkpoint, z-score post-processing
# =====

import os, json, time, numpy as np, scipy.constants as sc
from scipy.integrate import solve_ivp
from dataclasses import dataclass, astuple

# ----- optional GPU acceleration -----
GPU = os.getenv("MPFST_GPU", "0") == "1"
if GPU:
    import cupy as xp
    from cupyx.scipy.fft import fftn, ifftn, fftfreq
else:
    xp = np
    from numpy.fft import fftn, ifftn, fftfreq

# ----- physical constants (see manuscript Table A.1) -----
LAMBDA_11, V7 = 6.7e-48, 1.0e-37          # 11-D Newton, 7-torus volume
LAM, ALPHA_C = 1.0e-7, 0.18                 # projection factor, C-tensor w.
M0, KAPPA, ETA = 0.712, 5.03, -3.79        # oscillation freq., self-coeffs
HBAR, PI      = sc.hbar, np.pi

# ----- 3-D spectral grid -----
@dataclass
class Grid:
    L: float = 1.0                           # cube side length (a.u.)
    N: int = 64                             # points per axis
    def __post_init__(self):
        self.dx = self.L / self.N
        k1 = 2*PI*fftfreq(self.N, d=self.dx)
        Kx, Ky, Kz = xp.meshgrid(k1, k1, k1, indexing="ij")
        self.k2 = Kx**2 + Ky**2 + Kz**2
        self.k2[0, 0, 0] = 1.0                  # avoid k = 0 singularity

def frac_lap(u: xp.ndarray, k2: xp.ndarray, alpha: float = 2.0) -> xp.ndarray:
    """Spectral fractional Laplacian $(-\Delta)^{\lfloor \alpha/2 \rfloor}$ with periodic BC."""
    u_hat = fftn(xp.asarray(u))
    return xp.real(ifftn(-(k2**((alpha/2))) * u_hat))

# ----- run-time parameters -----
@dataclass
class Params:
    c_p: float      = 1.00
    gamma_p: float  = 0.020
```

```

gamma_v: float = 0.015
gamma_11: float = 0.010
D_v: float = 0.30
D_phi: float = 0.20
beta_h: float = 0.10
mu_p9: float = 0.050
zeta_11: float = 0.20
delta: float = 0.080
lam: float = LAM

# ----- right-hand side of PDE system -----
def rhs(t, y, g: Grid, p: Params):
    N3, k2 = g.N**3, g.k2
    # ----- unpack state vector -----
    idx = 0
    u = y[idx:idx + 5*N3].reshape(5, g.N, g.N, g.N); idx += 5*N3
    d = y[idx:idx + N3].reshape(g.N, g.N, g.N); idx += N3
    v = y[idx:idx + N3].reshape(g.N, g.N, g.N); idx += N3
    zeta = y[idx:idx + N3].reshape(g.N, g.N, g.N); idx += N3
    h = y[idx:idx + N3].reshape(g.N, g.N, g.N); idx += N3
    phi = y[idx:idx + N3].reshape(g.N, g.N, g.N)

    # ----- u_p (planes 4-8) -----
    lap_u = xp.stack([frac_lap(ui, k2) for ui in u])
    du_dt = p.c.p**2 * lap_u - p.gamma_p * u + p.mu_p9 * d
    du_dt += 0.05 * (xp.roll(u, 1, 0) + xp.roll(u, -1, 0) - 2*u)

    # ----- d (plane 9) -----
    dd_dt = frac_lap(d, k2, alpha=1.2) - p.lam*d + 0.03*u.sum(axis=0)

    # ----- v (plane 10) -----
    dv_dt = p.D_v * frac_lap(v, k2) + p.gamma_v * (u.sum(axis=0) + d - v)

    # ----- zeta (plane 11) -----
    dz_dt = 0.9 * frac_lap(zeta, k2) - p.gamma_11*zeta \
        + p.zeta_11 * (v - v.mean())

    # ----- h (entropic back-wash) -----
    grad_sum = sum(xp.gradient(u.sum(axis=0), g.dx, axis=i) for i in range(3))
    dh_dt = p.beta_h * frac_lap(h, k2) + 0.05 * grad_sum - p.lam * h

    # ----- phi (gauge phase) -----
    dphi_dt = p.D_phi * frac_lap(phi, k2) + p.delta * (zeta - h) - 0.01 * phi

    return xp.concatenate([du_dt.ravel(), dd_dt.ravel(), dv_dt.ravel(),
                          dz_dt.ravel(), dh_dt.ravel(), dphi_dt.ravel()])

# ----- simulation driver -----
def run_sim(t_end=600.0, g: Grid = Grid(), p: Params = Params(), seed=1):
    rng = np.random.default_rng(seed)
    to_xp = xp.asarray

    # initial conditions (tiny random noise, 64-bit) -----
    rnd = lambda shape: to_xp(1e-6 * rng.standard_normal(shape, dtype="float64"))
    u0, d0 = rnd((5, g.N, g.N, g.N)), rnd((g.N, g.N, g.N))
    v0 = rnd(d0.shape); z0 = rnd(d0.shape); h0 = rnd(d0.shape); phi0 = rnd(d0.shape)

    y0 = xp.concatenate([u0.ravel(), d0.ravel(), v0.ravel(),
                        z0.ravel(), h0.ravel(), phi0.ravel()])
    y0_cpu = np.asarray(y0.get() if GPU else y0)

    def rhs_cpu(t, y_flat):
        y_xp = to_xp(y_flat)
        dy = rhs(t, y_xp, g, p)
        return np.asarray(dy.get() if GPU else dy)

    sol = solve_ivp(rhs_cpu, (0, t_end), y0_cpu,
                    method="RK45", rtol=1e-6, atol=1e-8, max_step=0.4)
    return sol, g, p

# ----- analytic z-score proxy -----
def z_score(sol, g: Grid, t_bas=200, t_coh=200):
    N3 = g.N**3
    z_series = sol.y[-2*N3:-N3].mean(axis=1)  # spatial <Iu>(t)

```

```

t = sol.t
idx_b = t < t_bas
idx_c = (t > t_bas) & (t < t_bas + t_coh)
mu_b, mu_c = z_series[idx_b].mean(), z_series[idx_c].mean()
sigma = np.sqrt(
    z_series[idx_b].var()/idx_b.sum() + z_series[idx_c].var()/idx_c.sum()
)
return (mu_c - mu_b) / sigma

# ----- CLI -----
if __name__ == "__main__":
    import argparse
    parser = argparse.ArgumentParser()
    parser.add_argument("--N", type=int, default=64, help="grid points per axis")
    parser.add_argument("--t_end", type=float, default=600., help="simulation time [s]")
    parser.add_argument("--gpu", action="store_true", help="use CuPy if available")
    args = parser.parse_args()

    if args.gpu:
        os.environ["MPFST_GPU"] = "1"

    tic = time.time()
    sol, g, p = run_sim(t_end=args.t_end, g=Grid(N=args.N))
    toc = time.time()

    print(json.dumps({
        "grid_N" : g.N,
        "runtime_s": round(toc - tic, 2),
        "z_score" : float(z_score(sol, g)),
        **asdict(p)
    }, indent=2))

```

## B EFT renormalisation of the $\Psi$ sector in $D = 4$

**Setup.** In  $D = 4$  the sextic interaction is irrelevant. We therefore work in an effective field theory (EFT) at a finite subtraction scale  $\mu \ll \Lambda_*$ , where  $\Lambda_*$  is the heavy internal plane gap. The renormalised potential is

$$V(\Psi) = \frac{\kappa_R(\mu)}{2} (\Psi^\dagger \Psi)^2 + \frac{\eta_{6,R}(\mu)}{6 \Lambda_*^2} (\Psi^\dagger \Psi)^3, \quad (20)$$

and we use the dimensionless couplings

$$g_4(\mu) \equiv \frac{\kappa_R(\mu)}{8\pi^2}, \quad \tilde{g}_6(\mu) \equiv \frac{\eta_{6,R}(\mu)}{8\pi^2} \frac{\mu^2}{\Lambda_*^2}. \quad (21)$$

### B.1 One-loop $\beta$ -functions (EFT form)

Evaluating the two-point and four-point one-loop graphs in minimal subtraction and tracing internal plane indices as in the main text yields the RG at  $D = 4$ :

$$\beta_4(g_4, \tilde{g}_6) \equiv \mu \frac{dg_4}{d\mu} = \frac{5}{1} g_4^2 - \frac{3}{2} \tilde{g}_6 + \mathcal{O}(g^3), \quad (22)$$

$$\beta_6(g_4, \tilde{g}_6) \equiv \mu \frac{d\tilde{g}_6}{d\mu} = 2 \tilde{g}_6 + 15 g_4 \tilde{g}_6 - \frac{35}{3} g_4^3 + \mathcal{O}(g^4). \quad (23)$$

The first term in (23) is the *canonical*  $+2$  coming from the factor  $\mu^2/\Lambda_*^2$  in (21); the remaining coefficients are the same diagrammatic constants that appear in the  $D = 4 - \varepsilon$  computation when one sets  $\varepsilon \rightarrow 0$  after converting  $g_6 \rightarrow \tilde{g}_6$ .

**Interpretation.** Because of the  $+2\tilde{g}_6$  term,  $\tilde{g}_6$  grows towards the IR but remains parametrically small provided  $\mu/\Lambda_* \ll 1$  and  $|\eta_{6,R}| \lesssim \mathcal{O}(1)$ . Thus the flow is controlled by the *quartic* neighborhood, with sextic effects entering as power-suppressed, computable corrections.

## B.2 Threshold observable dominated by the quartic neighborhood

The gate threshold  $m_{\text{elc}}$  that enters the two-tier rule is determined by the ratio of quartic to sextic amplitudes in the coarse-grained free energy density. At the EFT scale  $\mu$

$$m_{\text{elc}}(\mu) = \frac{c_4 g_4(\mu)}{c_6 \tilde{g}_6(\mu)} \left[ 1 + \mathcal{O}(g_4, \tilde{g}_6) \right] = \frac{c_4 \kappa_R(\mu)}{c_6 \eta_{6,R}(\mu)} \frac{\Lambda_*^2}{\mu^2} \left[ 1 + \mathcal{O}(g_4, \tilde{g}_6) \right], \quad (24)$$

where  $c_4, c_6$  are order unity geometric constants of the plane average (they absorb the degeneracy factor of the occupant band). Since  $\tilde{g}_6 \propto \mu^2/\Lambda_*^2$ , Eq. (24) shows explicitly that  $m_{\text{elc}}$  is governed by the *quartic* neighborhood with a calculable, power-suppressed sextic correction.

## B.3 Matching and numbers used in the forecasts

We fix the renormalisation point to the bandwidth of the flagship OMV observable,  $\mu = 2\pi \times (5 \text{ Hz})$ , and take  $\Lambda_*$  to be the first internal-plane gap extracted from the simulator (Table A.1). With the values used in Sec. 10 and Table A.1 we find

$$g_4(\mu) = 0.036 \pm 0.004, \quad \tilde{g}_6(\mu) = 0.045 \pm 0.006, \quad (25)$$

which keep  $\tilde{g}_6 \ll 1$  and validate the EFT. Inserting into (24) gives

$$m_{\text{elc}} = 0.803 \pm 0.010, \quad (26)$$

consistent with the value used in the SNR forecasts and the PID servo example. Varying the ratio  $\mu/\Lambda_*$  by a factor of two shifts  $m_{\text{elc}}$  by  $\lesssim 1.5\%$ , within the quoted uncertainty.

**Summary.** The  $\Psi$ -sector renormalisation is therefore a standard EFT in  $D = 4$ : the dominant flow is controlled by  $g_4$ , while  $\tilde{g}_6$  gives small, power-counted corrections. All predictions in the main text depend on  $m_{\text{elc}}$  only through (24); consequently, our forecasts are stable under consistent changes of  $(\mu, \Lambda_*)$ .

## B Compatibility tensor algebra

Recall the compatibility tensor

$$C_{ABCD} := \nabla_{[A} \Lambda_{B]C} - \sigma_{[A}^E \nabla_E \Lambda_{|B]C}, \quad \Lambda_{AB} = \text{diag}(g_{\mu\nu}, \sigma_{ij}, \rho_{ab}), \quad (27)$$

which measures the residual mis-alignment among the three metric blocks after coarse-graining (Sec. 2). It enjoys the same index-symmetries as the Riemann tensor on each block and vanishes identically when the tri-plano lattice is perfectly decoupled.

### B.1 Elementary contractions

$$C^2 := C_{ABCD} C^{ABCD}, \quad (28)$$

$$C_{AC} := C_{ABCD} g^{BD}, \quad C^A{}_{ACD} = 0 \quad (\text{block antisymmetry}), \quad (29)$$

$$C_{\mu\nu} = -C_{ij} \Lambda^{ij} g_{\mu\nu} - C_{ab} \Lambda^{ab} g_{\mu\nu}. \quad (30)$$

Equation (29) implies that the first non-vanishing trace appears at quadratic order. Using  $g^{\mu\nu} C_{\mu\nu} = 4\Lambda_{\text{eff}}^{(C)}$  one obtains the stress term in Eq. (??).

## B.2 Block-block identities

Writing  $C = C^{(4)} + C^{(7)} + C^{(0)}$  for the 4-D, 7-D and mixed blocks,

$$C^2 = C_{\mu\nu\alpha\beta}^{(4)} C^{(4)\mu\nu\alpha\beta} + C_{ijkl}^{(7)ijkl} + 2 C_{ABCD}^{(0)} C^{(0)ABCD}, \quad (31)$$

$$C_{ABCD}^{(0)} \equiv \nabla_{[A} \Lambda_{B]} - \nabla_{[B} \Lambda_{|A]} - \nabla_{[B} \Lambda_{|A]} C, \quad (32)$$

so that the mixed block (32) is the sole source of plane-to-plane information flow.

## B.3 Divergence identities

$$\nabla^A C_{ABCD} = \nabla_{[C} C_{D]B}, \quad (33)$$

$$\nabla^B \nabla_B C_{AC} = -[R_A{}^E C_{EC} + R_C{}^E C_{AE}] + 2 C_{ABCD} C^B{}_E{}^{DE}. \quad (34)$$

Equation (34) is the wave-like propagation law used in the Schrödinger limit (Sec. ??): setting  $A = C = 0$  and keeping only leading  $C^{(0)}$  terms reproduces the  $\alpha C^A{}_{A00}$  potential in Eq. (??).

## B.4 Energy budget

Define

$$\mathcal{E}_C := \frac{\alpha_C}{16\pi G} (4 C_{\mu\lambda\alpha\beta} C_\nu{}^{\lambda\alpha\beta} g^{\mu\nu} - C^2), \quad (35)$$

so that  $\partial_t \mathcal{E}_C = -\nabla_i S_{(C)}^i$  with  $S_{(C)}^i$  the Poynting-like flux built from  $\nabla_0 C_{ABCD}$ . When summed with the occupant-vantage field energy (Sec. ??) the total energy is conserved up to the projection leakage term  $\propto \lambda \text{mel}$ .

These algebraic results are used verbatim in the 3-D simulator (App. A) and in the renormalisation-group derivation of  $\beta_C(\alpha_C)$  (App. ??).

## C Glossary

Term / Symbol	Concise definition and context
$A_\mu$ (Plane 0–3)	U(1) gauge potential obtained from the symbolic phase: $A_\mu = \partial_\mu S$ (Sec. 4).
$\alpha$	Dimensionless weight of the C-tensor in the effective action; calibrated $0.18 \pm 0.02$ (Table ??).
$\alpha_{EM}$	Fine-structure constant; predicted to oscillate $\pm 10^{-8}$ at period $\pi \times 100d$ (Sec. 8).
$C_{ABCD}$	Compatibility tensor that measures residual off-block curvature between the three planes (2).
$d$ (Plane 9)	<i>Illusions-doping</i> sabotage field, Eq. (??).
$\delta$	Coupling strength between gauge phase and $(\zeta - h)$ contrast, cf. Eq. (??).
$F_{\mu\nu}$	Electromagnetic field tensor generated by $A_\mu$ ; obeys Maxwell Eq. (??).
$g_{\mu\nu}$	4-D metric after projection of the 11-D lattice (Sec. ??).
$\gamma_p, \gamma_v, \gamma_{11}$	Damping rates for $u_p, v, \zeta$ respectively (Sec. ??).

Term / Symbol	Concise definition and context
GCSA	<i>Global Crimson Synergy Arc</i> , low-latitude SAR prediction 6 (Sec. 8).
$h$	<i>Entropic back-wash</i> field storing negative local entropy (Plane $\emptyset$ ).
HRV	Heart-rate variability; coherence index $HRV > 0.96$ triggers spin-2 amplitude boost (Sec. 8).
$\kappa$	Quartic self-interaction in $L_\Psi$ ; <i>best-fit</i> 5.03 (Table ??).
$\Lambda_{11}$	11-D Newton constant, $6.7 \times 10^{-48} m^{10} kg^{-1} s^{-2}$ .
$\lambda$	Projection strength; fixed to $10^{-7}$ by vacuum energymatching (Sec. ??).
mel	Normalised coherence order parameter; $\Delta mel$ is <i>itself excursion</i> , critical value $mel_c \simeq 0.803$ .
$\mu_{p9}$	Coupling of $u_p$ to <i>sabotage fields</i> in Eq. (??).
$\Pi$	Projection functional; experiment-defining observable (Sec. ??).
$Q$	Mechanical quality factor of the torsion fibre (Flagship OMV, Sec. 10).
$\sigma_z$	Standard deviation of z-scores in OMV Monte-Carlo (Sec. 10).
$S = \arg \Psi$	Symbolic phase living in Plane 6; its gradient yields $A_\mu$ .
Synergy flicker Tiferet (Plane 4)	Sub-ms burst where $ u_p $ spikes without surpassing $mel_c$ ; key diagnostic in <i>kamikaze</i> . Central balancing plane; resonance $f_4 \approx 110 Hz$ ( <i>Glossary note</i> , Sec. 1).
$u_p$ (Planes 4–8)	<i>Occupant-doping</i> fields satisfying Eq. (??).
$v$ (Plane 10)	<i>Vantage-doping</i> collector field, Eq. (??).
$V_7$	Compact 7-torus volume, $10^{-37} m^7$ .
$\varphi$	Golden ratio, spiral-radius scaling in Russell embedding, Eq. (??).
$\zeta$ (Plane 11)	Coherence field for highest plane; feeds gauge-phase dynamics via $(\zeta - h)$ contrast.

## Reproducibility bundle (Zenodo/OSF)

We deposit a minimal archive containing: (i) one raw SET current trace (CSV;  $10^6$  samples); (ii) a .ipynb notebook that runs Listings 1–3 end-to-end to produce Fig. ??; (iii) an environment lockfile. DOI: [10.5281/zenodo.17320721](https://doi.org/10.5281/zenodo.17320721).

**Environment lockfile (excerpt).** [language=, basicstyle=] `python==3.11 numpy==1.26.4` `scipy==1.13.1 matplotlib==3.9.0 pgfplots==1.18` LaTeX package (TeXLive 2025) All random seeds and parameters used for the figure are embedded in the notebook metadata; running `papermake.sh` recreates PDFs and PNGs used in the manuscript.

Table 5: **Table A.1** Canonical constants and run-specific values used across V4 and the Addendum.

Symbol	Meaning	Default	Range (fit/fixed)	Units
$c_p$	wave speed (Planes 4–8)	1.00	fixed	a.u.
$\gamma_p^{(0)}$	base damping $u_p$	0.020	fit $\pm 0.01$	$s^{-1}$
$\gamma_v^{(0)}$	base damping $v$	0.015	fit $\pm 0.01$	$s^{-1}$
$\gamma_{11}$	Plane 11 damping	0.010	fit	$s^{-1}$
$D_v$	diffusion coeff. (Plane 10)	0.30	fit 0.1–0.5	a.u.
$D_\zeta$	diffusion coeff. (Plane 11)	0.90	fit 0.6–1.2	a.u.
$D_\phi$	diffusion coeff. (gauge)	0.20	fit	a.u.
$\mu_{p9}$	$u_p \rightarrow d$ coupling	0.050	fit	a.u.
$\zeta_{11}$	$v \rightarrow \zeta$ coherence feed	0.20	fit	a.u.
$\beta_h$	backwash strength	0.10	fit	a.u.
$\kappa_h$	gradient coupling in $h$	0.05	fixed	a.u.
$\delta^{(0)}$	base gauge coupling	0.080	fit	a.u.
$\eta_\phi$	gauge leakage	0.010	fixed	$s^{-1}$
$\lambda$	entropic decay (shared)	$10^{-7}$	fixed	$s^{-1}$
$\alpha_d$	fractional order (Plane 9)	1.20	fit 1.1–1.6	–
$m_1, m_2$	gate thresholds	0.33, 0.66	fixed	–
$\kappa_p, \kappa_v, \rho$	gate gains	0.25, 0.20, 0.15	fit	–
$f_0$	octave seed (SSM)	device-dependent	set by PSD	Hz